ACS OMEGA

http://pubs.acs.org/journal/acsodf

Article

A Transparent Nano-Polycrystalline $ZnWO_4$ Thin-Film Scintillator for High-Resolution X-ray Imaging

Heon Yong Jeong, Ju Hyuk Lee, Sang Yoon Lee, Jaewoo Lee, and Sung Oh Cho*

Cite This: *ACS Omega* 2021, 6, 33224−33230

Read Online

ACCESS | Metrics & More | Article Recommendations | Supporting Information

ABSTRACT: Facile approaches for creating thin-film scintillators with high spatial resolutions and variable shapes are required to broaden the applicability of high-resolution X-ray imaging. In this study, a transparent nano-polycrystalline $ZnWO_4$ thin-film scintillator was fabricated by thermal evaporation for high-resolution X-ray imaging. The scintillator is composed of nano-sized grains smaller than the optical wavelength range to minimize optical scattering. The high transparency of the scintillators affords a sufficiently high spatial resolution to resolve the 2 μm line and space patterns when used in a high-resolution X-ray imaging system with an effective pixel size of 650 nm. The thermal evaporation method is a convenient approach for depositing thin and uniform films on complex substrates. $ZnWO_4$ thin-film scintillators with various shapes, such as pixelated and curved, were fabricated via thermal evaporation. The results show that the transparent nano-polycrystalline $ZnWO_4$ thin-film scintillator deposited through thermal evaporation has a potential for use in various high-resolution X-ray imaging applications.

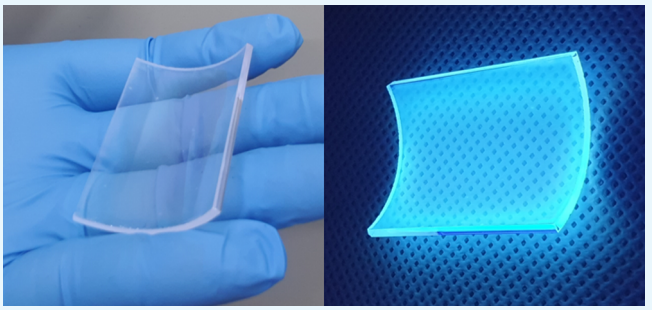

1. INTRODUCTION

High-resolution X-ray imaging is a promising technique in the field of X-ray microradiography for biological, archeological, material, and non-destructive analyses.[1−7] One of the most important parameters in high-resolution X-ray imaging is the spatial resolution[8−10] that is affected by the thickness of the scintillator because optical detectors with small effective pixel sizes are highly sensitive to the light-spread phenomenon.[11,12] To minimize light spread, several researchers have attempted to fabricate scintillators with several-micrometer-thin layers for high-resolution X-ray imaging.[8,13−15]

Powder screens and transparent films are typical forms of thin-layer scintillators. Powder-screen-type scintillators are commonly used because various scintillator shapes, such as pixelated and curved, can be fabricated easily using such scintillators.[16−18] Powder-screen scintillators are typically nanoparticle scintillators.[18−21] For powders with a particle size much larger than the optical wavelength range, however, the powder can significantly scatter the optical light generated by the scintillator, which reduces the spatial resolution of the resulting X-ray image.[19,22] However, the use of nanoparticle scintillators with particle sizes smaller than the optical wavelength range reduces the probability of optical light scattering, which increases the spatial resolution.[22−25]

Powder-screen scintillators are fundamentally limited by optical light diffusion.[8,24] To overcome this limitation, transparent film scintillators have been explored for high-resolution X-ray imaging.[26] Among relevant approaches, the liquid-phase epitaxial growth method is the most commonly employed technique.[27−30] Another approach is the one used by Kameshima *et al.*, who produced a transparent $Lu_3Al_5O_{12}$:Ce film scintillator on an undoped $Lu_3Al_5O_{12}$ substrate using a solid-state diffusion technique.[31] However, this method is complicated and requires additional processes such as cutting and polishing to prepare a thin and uniform film.[31] In addition, neither the liquid-phase epitaxial growth method nor the solid-state diffusion technique can produce thin-film scintillators with variable shapes.

Therefore, in this study, a transparent thin-film scintillator composed of nano-polycrystalline zinc tungstate ($ZnWO_4$) was fabricated on quartz glass using a thermal evaporation method with sintering. $ZnWO_4$ has been extensively used as a material for X-ray scintillators.[32,33] The reported light yield of $ZnWO_4$ (7000−9500 Ph/MeV)[34−36] is higher than that of the commercialized $Bi_4Ge_3O_{12}$.[33] In contrast, $ZnWO_4$ has lower emission intensity than recently reported inorganic scintillating and perovskite materials.[37,38] The perovskite scintillators are severely restricted due to their vulnerability to moisture and heat.[39,40] Furthermore, because $ZnWO_4$ has a much lower melting point than other inorganic scintillating materials, it can

Received: October 25, 2021
Accepted: November 15, 2021
Published: November 22, 2021

be efficiently used in the thermal evaporation method.[41,42] Additionally, $ZnWO_4$ has a high density (ρ = 7.87 g/cm^3), short decay time, high stability, and low cost.[32,43−45] Since $ZnWO_4$ has a high X-ray absorption capability,[44,46] it can be used in thin-film scintillators. There is a growing body of research on fabricating transparent ceramic thin films using thermal evaporation with sintering.[47−50] The thermal evaporation method is an efficient approach for conveniently depositing thin and uniform films on complex structures.[51−55] The main purpose of this study was to demonstrate that nanopolycrystalline $ZnWO_4$ thin-film scintillators can be utilized in high-resolution X-ray imaging. In addition, the proposed method can be used to fabricate thin-film scintillators with various shapes, thereby demonstrating its potential for use in different high-resolution X-ray imaging applications.

2. RESULTS AND DISCUSSION

2.1. $ZnWO_4$ Thin Films Deposited via Thermal Evaporation. When the $ZnWO_4$ powder fabricated by a solid-state reaction was irradiated by a 254 nm UV light, it emitted blue light (Figure 1a). Figure 1b shows the X-ray

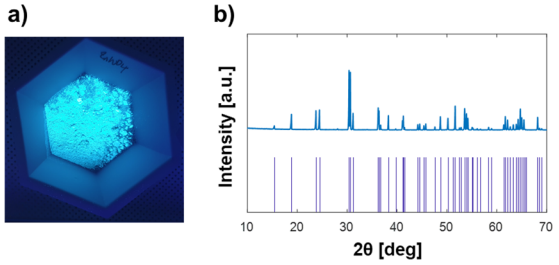

Figure 1. (a) $ZnWO_4$ powder irradiated with a 254 nm UV light and (b) the XRD spectrum of the $ZnWO_4$ powder.

diffraction (XRD) pattern of the $ZnWO_4$ powder. By comparing the peaks of the XRD pattern with the standard card (PDF ICDD card #01-078-0251), the powder was determined to be monoclinic crystalline $ZnWO_4$.

Bare $ZnWO_4$ thin films were deposited through thermal evaporation using the crystallized $ZnWO_4$ powder as the source material. Cross-sectional scanning electron microscopy (SEM) imaging revealed the grain-free structure of the bare $ZnWO_4$ thin films (Figure 2a), which contained no cracks or pores.

Figure 2b shows the energy-dispersive X-ray (EDX) spectrum obtained for a bare $ZnWO_4$ thin film; this spectrum shows peaks attributed to zinc, tungsten, and oxygen, as well as those attributed to silicon from the quartz glass. As shown in the XRD pattern in Figure 2c, no diffraction peaks were observed from the bare $ZnWO_4$ thin film, indicating an amorphous structure. Figure 2d shows the surface roughness of the film analyzed by atomic force microscopy (AFM). The root-mean-square (RMS) surface roughness was measured to be 1.74 nm, indicating that the bare $ZnWO_4$ thin film was highly uniform. The thin film was sintered at 700 °C and the surface roughness of the film was analyzed using AFM, and the RMS roughness was measured to be 8.90 nm (Figure S1). Since the bare $ZnWO_4$ thin film has a highly uniform surface, the sintered thin film also has sufficient uniformity.

2.2. Sintered $ZnWO_4$ Thin Films. Figure 3a shows photographs of the 3 μm-thick $ZnWO_4$ thin films sintered at 600, 700, 800, and 900 °C with 254 nm UV irradiation. Figure

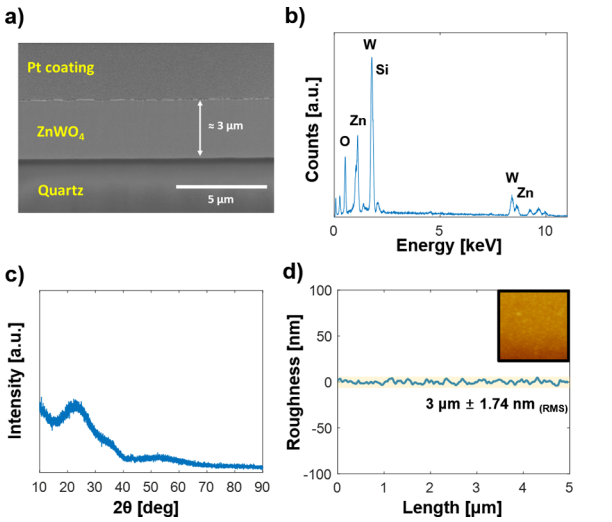

Figure 2. (a) Cross-sectional SEM image of a bare $ZnWO_4$ thin film obtained via focused ion beam milling. (b) EDX spectrum, (c) XRD pattern, and (d) AFM surface morphology (inset) and roughness of the bare $ZnWO_4$ thin film.

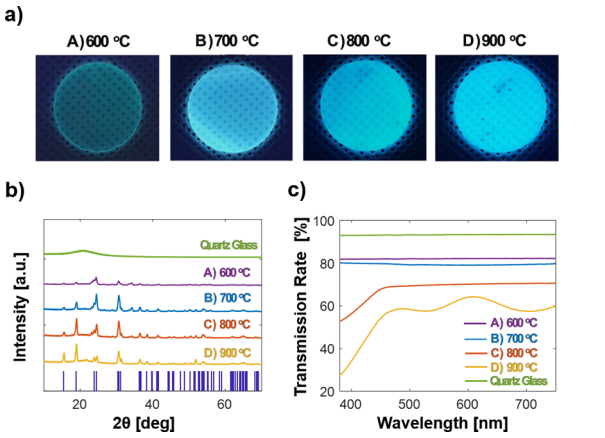

Figure 3. (a) Photographs of $ZnWO_4$ thin films sintered with 254 nm UV irradiation, (b) XRD patterns, and (c) transmission rate spectra of the $ZnWO_4$ thin films sintered at (A) 600, (B) 700, (C) 800, and (D) 900 °C; panels (b) and (c) also show the results for bare quartz glass.

3b presents the XRD patterns of the films, which show that they crystallized into pure monoclinic $ZnWO_4$. Figure 3c shows the transmission rate spectra of the films in the wavelength range of 200−800 nm. The most transparent samples were the films sintered at 600 and 700 °C, which exhibited transmission rates of 81 and 78%, respectively, at 480 nm. In contrast, the $ZnWO_4$ thin films sintered at 800 and 900 °C exhibited transmission rates of 68 and 56%, respectively, at 480 nm.

The structural morphologies determined through field emission scanning electron microscopy (FE-SEM) of the $ZnWO_4$ thin films sintered at different temperatures are shown in Figure 4. After sintering, the amorphous film became crystallized. For the $ZnWO_4$ thin film sintered at 900 °C, many pores and cracks on the scale of the wavelengths of optical light were formed (Figure 4d), which can reduce film transparency.[56,57] In other words, optical light scattering would occur if this film was used as a scintillator, which would reduce the spatial resolution of the resulting X-ray image.

https://doi.org/10.1021/acsomega.1c05962
ACS Omega 2021, 6, 33224−33230

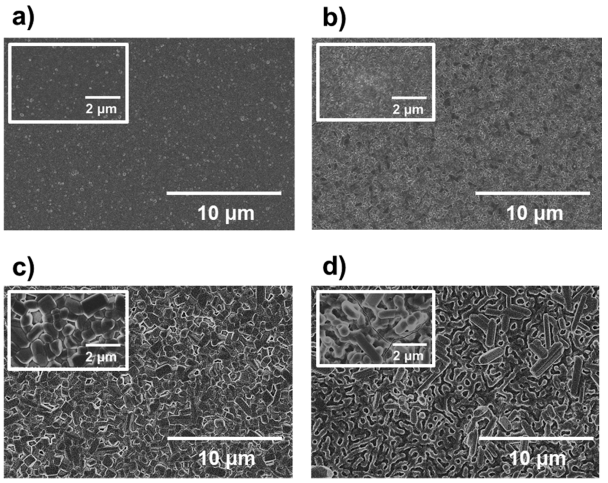

Figure 4. SEM images of the $ZnWO_4$ thin films sintered at (a) 600, (b) 700, (c) 800, and (d) 900 °C.

The $ZnWO_4$ thin films sintered at 600, 700, and 800 °C were composed of polycrystalline structures. The average grain sizes measured by FE-SEM using the intercept technique were 92.6, 157.3, and 698.7 nm for the films sintered at 600, 700, and 800 °C, respectively. Thus, the grain size increased with increasing sintering temperature.

The differences between the transmission rates of the thin films can be explained based on Mie scattering theory. When the grain size is comparable to the wavelengths of optical light, Mie scattering occurs at the grain boundaries.[58,59] However, when the grain size is sufficiently smaller than the wavelengths of optical light, Mie scattering is suppressed, allowing optical light to penetrate the film.[59−62] Therefore, the $ZnWO_4$ thin films sintered at 600 and 700 °C, with grains smaller than the optical wavelength range, were the most transparent.

The sintered $ZnWO_4$ thin films were irradiated with X-ray and UV light to evaluate their luminescent properties (Figure 5). For the thin films sintered at 700, 800, and 900 °C,

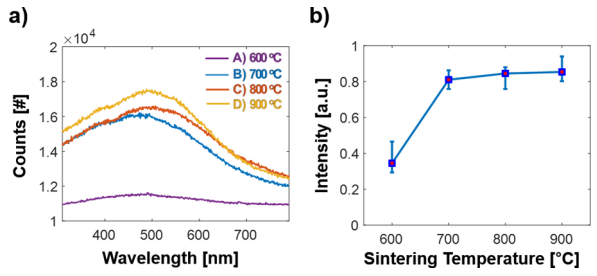

Figure 5. (a) Photoluminescence spectra under 325 nm UV irradiation and (b) emission intensities under X-ray irradiation of the $ZnWO_4$ thin-film scintillators sintered at 600, 700, 800, and 900 °C (the error bars represent the standard deviations of 20 independent measurements).

relatively high-intensity light emission was obtained without any significant differences between samples because the amorphous films were all completely crystallized. The emission intensity of the $ZnWO_4$ thin film sintered at 600 °C was lower than those of the films sintered at 700, 800, and 900 °C because in the former, the amorphous film did not completely change into a crystallized structure (Figure 3b). Thus, although the $ZnWO_4$ thin film sintered at 600 °C had the best transparency, it would be impossible to utilize as a scintillator.

The emission intensity of the film sintered at 800 °C was approximately 3.7% higher than that of the film sintered at 700 °C. However, since the latter had a smaller grain size, less optical light scattering would occur; thus, the spatial resolution, an important factor for high-resolution X-ray imaging, would increase. Hence, the film sintered at 700 °C with an average grain size of 157.3 nm was selected as the optimal.

2.3. Evaluation of High-Resolution X-ray Imaging Performance. A conventional nanoparticle screen scintillator was also manufactured, and its spatial resolution was compared with that of the nano-polycrystalline thin film in a high-resolution X-ray imaging system. The $ZnWO_4$ nanoparticle screen scintillator was fabricated using a solid-state reaction and drop-casting, and the particle size was similar to the grain size of the optimal nano-polycrystalline $ZnWO_4$ film.[22] The structures of the nano-polycrystalline film and nanoparticle screen are depicted in the SEM images in Figure 6. In the

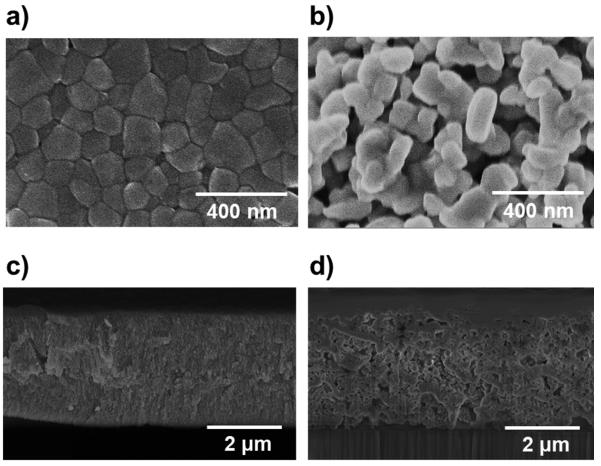

Figure 6. Surface SEM images of the (a) nano-polycrystalline $ZnWO_4$ film scintillator and (b) $ZnWO_4$ nanoparticle screen scintillator. Cross-sectional SEM images of the (c) nano-polycrystalline $ZnWO_4$ film scintillator and (d) $ZnWO_4$ nanoparticle screen scintillator.

nanoparticle screen, the particles were separated by air gaps. The optical light generated from the scintillator became scattered due to the difference in the refractive index of the particles and the air in the aforementioned gaps. In the nano-polycrystalline film, however, there were no gaps, because the nano-grains were closely packed. Consequently, there was no difference in refractive index at the grain boundaries, and thus, optical light scattering was suppressed.[63]

A schematic of the high-resolution X-ray imaging system is shown in Figure 7a. Figures 7b,c shows X-ray images of a 1500 mesh transmission electron microscopy (TEM) grid obtained from the high-resolution X-ray imaging system using the nanoparticle screen and nano-polycrystalline film scintillators, respectively. The modulation transfer function (MTF) graphs show that the spatial frequency of the nanoparticle screen and nano-polycrystalline film at the MTF value of 10% were 239 and 291 lp/mm, respectively (Figure S2a). Therefore, the spatial resolution provided by the nano-polycrystalline film was better than that of the nanoparticle screen scintillator. A high-resolution X-ray image of the JIMA RT RC-02 test pattern (JIMA, Chiyodaku, Japan) was developed using the nano-polycrystalline film (Figure 7d). The image confirms the better spatial resolution of the nano-polycrystalline film (Figure S2b),

https://doi.org/10.1021/acsomega.1c05962
ACS Omega 2021, 6, 33224−33230

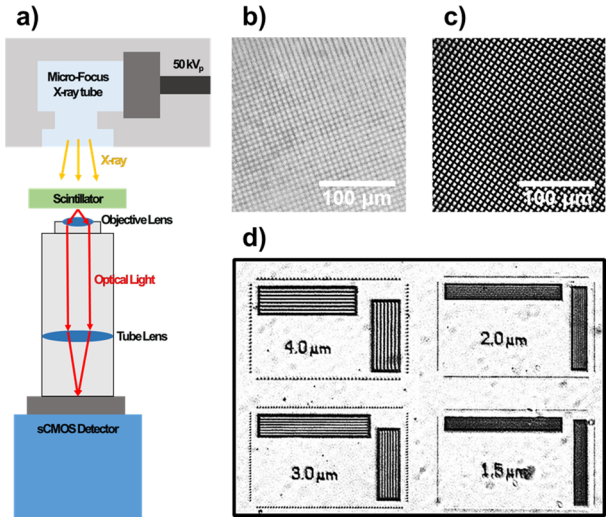

Figure 7. (a) Schematic of the high-resolution X-ray imaging system. High-resolution X-ray images of a 1500 mesh TEM grid obtained using the (b) nanoparticle screen scintillator and (c) nano-polycrystalline film scintillator. (d) High-resolution X-ray image of the JIMA RT RC-02 test pattern developed using the nano-polycrystalline film scintillator.

and the nano-polycrystalline transparent $ZnWO_4$ thin-film scintillator can resolve 2 μm lines and spatial patterns.

The thermal evaporation method allowed for the fabrication of a pixelated scintillator (Figures 8a,b) and a curved

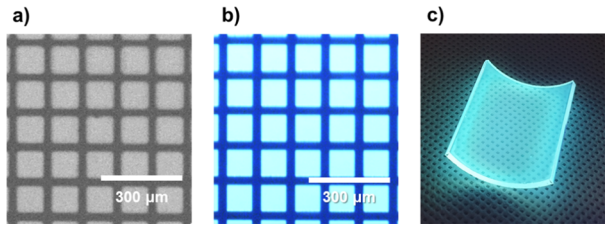

Figure 8. (a) SEM image of the pixelated scintillator and (b) optical microscopy image of the pixelated scintillator under 254 nm UV irradiation. (c) Curved scintillator under 254 nm UV irradiation.

scintillator (Figure 8c). The nano-polycrystalline $ZnWO_4$ film scintillator was deposited on quartz substrates using a micro-patterning mask (Figure 8a). The thickness of the pixelated scintillator can be increased to prevent light spread, as shown in Figure 8b; this can increase the X-ray sensitivity due to minimized light loss.[64] Figure 8c shows the curved $ZnWO_4$ thin-film scintillator under 254 nm UV irradiation. Curved scintillators are advantageous in that they can minimize distortion at the edge of X-ray images acquired via computed tomography (CT).[65,66] The curved transparent $ZnWO_4$ thin-film scintillator fabricated in this study could be used effectively in micro-CT because it has a high spatial resolution for X-ray micro-images without any distortion at the edges.

3. CONCLUSIONS

A nano-polycrystalline transparent $ZnWO_4$ thin-film scintillator was fabricated by thermal evaporation and was successfully utilized in high-resolution X-ray imaging. Since it has an average grain size of 157.3 nm, which is less than the optical wavelength, optical light scattering is suppressed. The optimal 3 μm-thick $ZnWO_4$ thin film exhibited high optical performance with a 480 nm transmission rate of 78%. The scintillator was analyzed using a high-resolution X-ray imaging system composed of a micro-focus X-ray tube, optical lens, and scientific complementary metal-oxide semiconductor (sCMOS) detector with an effective pixel size of 650 nm. An X-ray image of 2 μm line and space patterns was successfully resolved by the prepared scintillator. In addition, the demonstrated thermal evaporation method represents a convenient approach for fabricating thin-film scintillators with various shapes. Thus, the fabricated scintillators can be used in different high-resolution X-ray imaging applications. The demonstrated nano-polycrystalline transparent $ZnWO_4$ thin-film scintillator is expected to be useful in X-ray micro-radiography.

4. METHODS

4.1. Fabrication of $ZnWO_4$ Thin Films. Zinc oxide (ZnO) and tungsten oxide (WO_3) nanoparticles were purchased from Sigma-Aldrich (St. Louis, MO, USA). The nanoparticles were added to ethanol at a 1:1 atomic ratio between zinc and tungsten. The solution was mixed via vibrating ball milling and was dried in air at 60 °C; the resulting powders were heated in an electric furnace at 1000 °C for 5 h to induce a solid-state reaction.

The $ZnWO_4$ powder fabricated by the solid-state reaction was used as the source material for thermal evaporation. A tungsten boat was used as the evaporating crucible, and deposition on quartz glass (B&C Tech, Daejeon, South Korea) was performed at approximately 10^{-6} Torr. The holder was rotated 25 cm away from the crucible. After deposition, the bare $ZnWO_4$ thin films were sintered in an air furnace at 600, 700, 800, or 900 °C for 3 h.

4.2. Characterization. Cross-sectional samples of the bare $ZnWO_4$ thin films were prepared using a focused ion beam (FIB; Helios 450 F1, FEI, Hillsboro, OR, USA) and were analyzed using an SEM microscope and an EDX detector equipped in FIB. The crystallinity of the bare $ZnWO_4$ thin films was analyzed using XRD (D/MAX-2500, Rigaku, Tokyo, Japan) in the 2θ range of 10−70°. The surface structure was determined using an AFM instrument (XE70, Park systems, Suwon, Korea).

The structures of the sintered $ZnWO_4$ thin films were analyzed using FE-SEM (FEI MAGELLAN 400, FEI, Hillsboro, OR, USA), and the crystallization and transparency of the thin films were analyzed using XRD and a UV−vis/NIR spectrophotometer (Lambda 1050, Perkin Elmer, Massachusetts, USA). The photoluminescence (PL) spectra were obtained on a PL spectrometer (RAMBOSS-Star, DONGWOO OddPTRON, Gyeonggi-do, Korea) equipped with a UV laser (325 nm He-Cd Laser, Kimmon, Tokyo, Japan).

4.3. High-Resolution X-ray Imaging. The fabricated films were incorporated into a high-resolution X-ray imaging system comprising a micro-focus X-ray tube (P030-24-12F100W, Petrick GmbH, Bad Blankenburg, Germany), optical lens, and a sCMOS detector (pico.edge 4.2, PCO, Kelheim, Germany). The operating voltage and current of the micro-focus X-ray tube were set to 50 kV_p and 1 mA, respectively, and the focal spot size was 30−55 μm. A 10× optical lens was used to magnify the X-ray image on the scintillator film, and the sCMOS detector with a square pixel size of 6.5 μm × 6.5 μm was used to develop the image. The effective pixel size of this system coupled with the optical lens was 650 nm. The emission intensity of the scintillator was

https://doi.org/10.1021/acsomega.1c05962
ACS Omega 2021, 6, 33224−33230

measured by averaging the pixel values of the X-ray images developed in the high-resolution X-ray imaging system. The MTF was analyzed using the Fourier transform of the ESF data obtained from the high-resolution X-ray image of an edge of the 0.5-cm-thick tungsten block for comparing spatial resolution.

■ ASSOCIATED CONTENT

Supporting Information

The Supporting Information is available free of charge at https://pubs.acs.org/doi/10.1021/acsomega.1c05962.

(Figure S1) AFM surface morphology and roughness of the $ZnWO_4$ thin film, (Figure S2) MTF curves and a high-resolution X-ray image (PDF)

■ AUTHOR INFORMATION

Corresponding Author

Sung Oh Cho − *Department of Nuclear and Quantum Engineering, Korea Advanced Institute of Science and Technology, Daejeon 34141, Republic of Korea*; Email: socho@kaist.ac.kr

Authors

Heon Yong Jeong − *Department of Nuclear and Quantum Engineering, Korea Advanced Institute of Science and Technology, Daejeon 34141, Republic of Korea*

Ju Hyuk Lee − *Department of Nuclear and Quantum Engineering, Korea Advanced Institute of Science and Technology, Daejeon 34141, Republic of Korea*

Sang Yoon Lee − *Department of Nuclear and Quantum Engineering, Korea Advanced Institute of Science and Technology, Daejeon 34141, Republic of Korea*

Jaewoo Lee − *Department of Nuclear and Quantum Engineering, Korea Advanced Institute of Science and Technology, Daejeon 34141, Republic of Korea*

Complete contact information is available at: https://pubs.acs.org/10.1021/acsomega.1c05962

Author Contributions

The manuscript was written through contributions of all authors. All authors have given approval to the final version of the manuscript.

Funding

This work was supported by the National Research Foundation of Korea (NRF) grant funded by the Korea government (NRF-2020M2D8A206972712).

Notes

The authors declare no competing financial interest.

■ ACKNOWLEDGMENTS

This research was funded by a National Research Foundation of Korea (NRF) grant funded by the Korean government (NRF-2020M2D8A206972712).

■ REFERENCES

(1) Mizutani, R.; Suzuki, Y. X-ray microtomography in biology. *Micron* **2012**, *43*, 104−115.

(2) Dudak, J.; Zemlicka, J.; Karch, J.; Patzelt, M.; Mrzilkova, J.; Zach, P.; Hermanova, Z.; Kvacek, J.; Krejci, F. High-contrast X-ray micro-radiography and micro-CT of ex-vivo soft tissue murine organs utilizing ethanol fixation and large area photon-counting detector. *Sci. Rep.* **2016**, *6*, 30385−30389.

(3) Adderley, W. P.; Simpson, I. A.; MacLeod, G. W. Testing high-resolution X-ray computed tomography for the micromorphological analyses of archaeological soils and sediments. *Archaeol. Prospect.* **2001**, *8*, 107−112.

(4) Vandiver, P. B.; Ellingson, W. A.; Robinson, T. K.; Lobick, J. J.; Séguin, F. H. New applications of X-radiographic imaging technologies for archaeological ceramics. *Archeomaterials* **1991**, *5*, 185−207.

(5) Zschech, E.; Yun, W.; Schneider, G. High-resolution X-ray imaging—a powerful nondestructive technique for applications in semiconductor industry. *Appl. Phys. A: Mater. Sci. Process.* **2008**, *92*, 423−429.

(6) Ketcham, R. A.; Iturrino, G. J. Nondestructive high-resolution visualization and measurement of anisotropic effective porosity in complex lithologies using high-resolution X-ray computed tomography. *J. Hydrol.* **2005**, *302*, 92−106.

(7) Cao, J.; Guo, Z.; Zhu, S.; Fu, Y.; Zhang, H.; Wang, Q.; Gu, Z. Preparation of lead-free two-dimensional-layered $(C_8H_{17}NH_3)_2SnBr_4$ perovskite scintillators and their application in x-ray imaging. *ACS Appl. Mater. Interfaces* **2020**, *12*, 19797−19804.

(8) Martin, T.; Koch, A. Recent developments in X-ray imaging with micrometer spatial resolution. *J. Synchrotron Radiat.* **2006**, *13*, 180−194.

(9) Kobayashi, M.; Komori, J.; Shimidzu, K.; Izaki, M.; Uesugi, K.; Takeuchi, A.; Suzuki, Y. Development of vertically aligned ZnO-nanowires scintillators for high spatial resolution x-ray imaging. *Appl. Phys. Lett.* **2015**, *106*, No. 081909.

(10) Touš, J.; Horvath, M.; Pína, L.; Blažek, K.; Sopko, B. High-resolution application of YAG: Ce and LuAG: Ce imaging detectors with a CCD X-ray camera. *Nucl. Instrum. Methods Phys. Res., Sect. A* **2008**, *591*, 264−267.

(11) Cha, B. K.; Lee, D. H.; Kim, B.; Seo, C.-W.; Jeon, S.; Huh, Y.; Kim, J. Y.; Cho, G.; Kim, Y. High-resolution X-ray imaging based on pixel-structured CsI: Tl scintillating screens for indirect X-ray image sensors. *J. Korean Phys. Soc.* **2011**, *59*, 3670−3673.

(12) Howansky, A.; Lubinsky, A. R.; Suzuki, K.; Ghose, S.; Zhao, W. An apparatus and method for directly measuring the depth-dependent gain and spatial resolution of turbid scintillators. *Med. Phys.* **2018**, *45*, 4927−4941.

(13) Cecilia, A.; Rack, A.; Douissard, P.-A.; Martin, T.; dos Santos Rolo, T.; Vagovič, P.; Hamann, E.; Van de Kamp, T.; Riedel, A.; Fiederle, M. LPE grown LSO: Tb scintillator films for high-resolution X-ray imaging applications at synchrotron light sources. *Nucl. Instrum. Methods Phys. Res., Sect. A* **2011**, *648*, S321−S323.

(14) Tous, J.; Blazek, K.; Nikl, M.; Mares, J. In *Single crystal scintillator plates used for light weight material X-ray radiography*; Journal of Physics: Conference Series, IOP Publishing: 2013; p 192017.

(15) Li, G.; Luo, S.; Yan, Y.; Gu, N. A method of extending the depth of focus of the high-resolution X-ray imaging system employing optical lens and scintillator: a phantom study. *Biomed. eng. online* **2015**, *14*, 120−114.

(16) Jung, P. G.; Lee, C. H.; Bae, K. M.; Lee, J. M.; Lee, S. M.; Lim, C. H.; Yun, S.; Kim, H. K.; Ko, J. S. Microdome-gooved Gd $_2O_2S$: Tb scintillator for flexible and high resolution digital radiography. *Opt. Express* **2010**, *18*, 14850−14858.

(17) Cha, B. K.; Lee, S. J.; Muralidharan, P.; Kim, D. K.; Kim, J. Y.; Cho, G.; Jeon, S.; Huh, Y. Novel nanocrystalline Gd2O3 (Eu) scintillator screens with a micro-pixel structure for high spatial resolution X-ray imaging. *Nucl. Instrum. Methods Phys. Res., Sect. A* **2011**, *652*, 717−720.

(18) Sen, S.; Tyagi, M.; Sharma, K.; Sarkar, P. S.; Sarkar, S.; Basak, C. B.; Pitale, S.; Ghosh, M.; Gadkari, S. C. Organic−Inorganic Composite Films Based on $Gd_3Ga_3Al_2O_{12}$: Ce Scintillator Nanoparticles for X-ray Imaging Applications. *ACS Appl. Mater. Interfaces* **2017**, *9*, 37310−37320.

(19) Kang, Z.; Zhang, Y.; Menkara, H.; Wagner, B. K.; Summers, C. J.; Lawrence, W.; Nagarkar, V. CdTe quantum dots and polymer

nanocomposites for x-ray scintillation and imaging. *Appl. Phys. Lett.* **2011**, *98*, 181914.
(20) Zhang, Y.; Sun, R.; Ou, X.; Fu, K.; Chen, Q.; Ding, Y.; Xu, L.-J.; Liu, L.; Han, Y.; Malko, A. V.; Liu, X.; Yang, H.; Bakr, O. M.; Liu, H.; Mohammed, O. F. Metal halide perovskite nanosheet for X-ray high-resolution scintillation imaging screens. *ACS Nano* **2019**, *13*, 2520−2525.
(21) Sedov, V.; Kouznetsov, S.; Martyanov, A.; Proydakova, V.; Ralchenko, V.; Khomich, A.; Voronov, V.; Batygov, S.; Kamenskikh, I.; Spassky, D.; Savin, S.; Fedorov, P. Diamond−rare earth composites with embedded $NaGdF_4$: Eu nanoparticles as robust photo-and X-ray-luminescent materials for radiation monitoring screens. *ACS Appl. Nano Mater.* **2020**, *3*, 1324−1331.
(22) Jeong, H. Y.; Lim, H. S.; Lee, J. H.; Heo, J.; Kim, H. N.; Cho, S. O. $ZnWO_4$ Nanoparticle Scintillators for High Resolution X-ray Imaging. *Nanomaterials* **2020**, *10*, 1721.
(23) Cha, B. K.; Lee, S. J.; Muralidharan, P.; Kim, J. Y.; Kim, D. K.; Cho, G. Characterization and imaging performance of nanoscintillator screen for high resolution X-ray imaging detectors. *Nucl. Instrum. Methods Phys. Res., Sect. A* **2011**, *633*, S294−S296.
(24) Liaparinos, P. F. Optical diffusion performance of nano-phosphor-based materials for use in medical imaging. *J. Biomed. Opt* **2012**, *17*, 126013.
(25) Kumi Barimah, E.; Rahayu, S.; Ziarko, M. W.; Bamiedakis, N.; White, I. H.; Penty, R. V.; Kale, G. M.; Jose, G. Erbium-Doped Nanoparticle−Polymer Composite Thin Films for Photonic Applications: Structural and Optical Properties. *ACS Omega* **2020**, *5*, 9224−9232.
(26) Koch, A.; Raven, C.; Spanne, P.; Snigirev, A. X-ray imaging with submicrometer resolution employing transparent luminescent screens. *J. Opt. Soc. Am. A* **1998**, *15*, 1940−1951.
(27) Buryi, M.; Laguta, V.; Nikl, M.; Gorbenko, V.; Zorenko, T.; Zorenko, Y. LPE growth and study of the Ce^{3+} incorporation in $LuAlO_3$: Ce single crystalline film scintillators. *CrystEngComm* **2019**, *21*, 3313−3321.
(28) Martin, T.; Douissard, P.-A.; Couchaud, M.; Cecilia, A.; Baumbach, T.; Dupre, K.; Rack, A. LSO-based single crystal film scintillator for synchrotron-based hard X-ray micro-imaging. *IEEE Trans. Nucl. Sci.* **2009**, *56*, 1412−1418.
(29) Gorbenko, V.; Zorenko, T.; Witkiewicz, S.; Paprocki, K.; Sidletskiy, O.; Fedorov, A.; Bilski, P.; Twardak, A.; Zorenko, Y. LPE Growth of Single Crystalline Film Scintillators Based on Ce^{3+} Doped $Tb_{3-x}Gd_xAl_{5-y}Ga_yO_{12}$ Mixed Garnets. *Crystals* **2017**, *7*, 262.
(30) Witkiewicz-Lukaszek, S.; Gorbenko, V.; Zorenko, T.; Sidletskiy, O.; Arhipov, P.; Fedorov, A.; Mares, J. A.; Kucerkova, R.; Nikl, M.; Zorenko, Y. Liquid phase epitaxy growth of high-performance composite scintillators based on single crystalline films and crystals of LuAG. *CrystEngComm* **2020**, *22*, 3713−3724.
(31) Kameshima, T.; Takeuchi, A.; Uesugi, K.; Kudo, T.; Kohmura, Y.; Tamasaku, K.; Muramatsu, K.; Yanagitani, T.; Yabashi, M.; Hatsui, T. Development of an X-ray imaging detector to resolve 200 nm line-and-space patterns by using transparent ceramics layers bonded by solid-state diffusion. *Opt. Lett.* **2019**, *44*, 1403−1406.
(32) Garadkar, K.; Ghule, L.; Sapnar, K.; Dhole, S. A facile synthesis of $ZnWO_4$ nanoparticles by microwave assisted technique and its application in photocatalysis. *Mater. Res. Bull.* **2013**, *48*, 1105−1109.
(33) Oi, T.; Takagi, K.; Fukazawa, T. Scintillation study of $ZnWO_4$ single crystals. *Appl. Phys. Lett.* **1980**, *36*, 278−279.
(34) Klamra, W.; Szczesniak, T.; Moszynski, M.; Iwanowska, J.; Swiderski, L.; Syntfeld-Kazuch, A.; Shlegel, V. N.; Vasiliev, Y. V.; Galashov, E. N. Properties of $CdWO_4$ and $ZnWO_4$ scintillators at liquid nitrogen temperature. *J. Instrum.* **2012**, *7*, P03011.
(35) Kowalski, Z.; Kaczmarek, S. M.; Drozdowski, W.; Witkowski, M. E.; Makowski, M.; Brylew, K.; Berkowski, M.; Głowacki, M. Radioluminescence, low temperature thermoluminescence and scintillation properties of Ca and Eu doped $ZnWO_4$ single crystals. *Radiat. Meas.* **2018**, *118*, 1−7.
(36) Holl, I.; Lorenz, E.; Mageras, G. A measurement of the light yield of common inorganic scintillators. *IEEE Trans. Nucl. Sci.* **1988**, *35*, 105−109.
(37) He, Q.; Zhou, C.; Xu, L.; Lee, S.; Lin, X.; Neu, J.; Worku, M.; Chaaban, M.; Ma, B. Highly stable organic antimony halide crystals for X-ray scintillation. *ACS Mater. Lett.* **2020**, *2*, 633−638.
(38) Yanagida, T.; Kamada, K.; Fujimoto, Y.; Yagi, H.; Yanagitani, T. Comparative study of ceramic and single crystal Ce: GAGG scintillator. *Opt. Mater.* **2013**, *35*, 2480−2485.
(39) Habisreutinger, S. N.; McMeekin, D. P.; Snaith, H. J.; Nicholas, R. J. Research Update: Strategies for improving the stability of perovskite solar cells. *APL Mater.* **2016**, *4*, No. 091503.
(40) Zhang, H.; Yang, Z.; Zhou, M.; Zhao, L.; Jiang, T.; Yang, H.; Yu, X.; Qiu, J.; Yang, Y. M.; Xu, X. Reproducible X-ray Imaging with a Perovskite Nanocrystal Scintillator Embedded in a Transparent Amorphous Network Structure. *Adv. Mater.* **2021**, *33*, 2102529.
(41) Wang, X.; Fan, Z.; Yu, H.; Zhang, H.; Wang, J. Characterization of $ZnWO_4$ Raman crystal. *Opt. Mater. Express* **2017**, *7*, 1732−1744.
(42) Trots, D.; Senyshyn, A.; Vasylechko, L.; Niewa, R.; Vad, T.; Mikhailik, V.; Kraus, H. Crystal structure of $ZnWO_4$ scintillator material in the range of 3−1423 K. *J. Condens. Matter Phys.* **2009**, *21*, 325402.
(43) Grassmann, H.; Moser, H.-G.; Lorenz, E. Scintillation properties of $ZnWO_4$. *J. Lumin.* **1985**, *33*, 109−113.
(44) Dkhilalli, F.; Borchani, S. M.; Rasheed, M.; Barille, R.; Guidara, K.; Megdiche, M. Structural, dielectric, and optical properties of the zinc tungstate $ZnWO_4$ compound. *J. Mater. Sci.: Mater. Electron.* **2018**, *29*, 6297−6307.
(45) Kraus, H.; Mikhailik, V. B.; Ramachers, Y.; Day, D.; Hutton, K. B.; Telfer, J. Feasibility study of a $ZnWO_4$ scintillator for exploiting materials signature in cryogenic WIMP dark matter searches. *Phys. Lett. B* **2005**, *610*, 37−44.
(46) Khyzhun, O.; Bekenev, V.; Atuchin, V.; Galashov, E.; Shlegel, V. Electronic properties of $ZnWO_4$ based on ab initio FP-LAPW band-structure calculations and X-ray spectroscopy data. *Mater. Chem. Phys.* **2013**, *140*, 588−595.
(47) Bouhssira, N.; Abed, S.; Tomasella, E.; Cellier, J.; Mosbah, A.; Aida, M.; Jacquet, M. Influence of annealing temperature on the properties of ZnO thin films deposited by thermal evaporation. *Appl. Surf. Sci.* **2006**, *252*, 5594−5597.
(48) Lee, W.-J.; Cho, D.-H.; Do Kim, Y.; Choi, M.-W.; Choi, J. C.; Chung, Y.-D. Thermally evaporated amorphous InZnO thin film applicable to transparent conducting oxide for solar cells. *J. Alloys Compd.* **2019**, *806*, 976−982.
(49) Suhail, M. H.; Ibrahim, I. M.; Mohan Rao, G. Characterization and gas sensitivity of cadimum oxide thin films prepared by thermal evaporation technique. *J. Electron Devices* **2012**, *13*, 965−974.
(50) Fakhri, M. A. Annealing effects on opto-electronic properties of Ag_2O films growth using thermal evaporation techniques. *Int. J. Nanoelectron. Mater.* **2016**, *9*, 93−102.
(51) Vaynzof, Y. The future of perovskite photovoltaics—thermal evaporation or solution processing? *Adv. Energy Mater.* **2020**, *10*, 2003073.
(52) Jin, H.-C.; Abelson, J. R.; Erhardt, M. K.; Nuzzo, R. G. Soft lithographic fabrication of an image sensor array on a curved substrate. *J. Vac. Sci. Technol., B* **2004**, *22*, 2548−2551.
(53) Park, J.; Fujita, H.; Kim, B. Fabrication of metallic microstructure on curved substrate by optical soft lithography and copper electroplating. *Sens. Actuators A: Phys.* **2011**, *168*, 105−111.
(54) de León, A. G.; Dirix, Y.; Staedler, Y.; Feldman, K.; Hähner, G.; Caseri, W. R.; Smith, P. Method for fabricating pixelated, multicolor polarizing films. *Appl. Opt.* **2000**, *39*, 4847−4851.
(55) Pugliese, M.; Prontera, C. T.; Polimeno, L.; Lerario, G.; Giannuzzi, R.; Esposito, M.; Carallo, S.; Costa, D.; De Marco, L.; De Giorgi, M.; Gigli, G.; Sanvitto, S.; Maiorano, V. Highly Reflective Periodic Nanostructure Based on Thermal Evaporated Tungsten Oxide and Calcium Fluoride for Advanced Photonic Applications. *ACS Appl. Nano Mater.* **2020**, *3*, 10978−10985.

https://doi.org/10.1021/acsomega.1c05962
ACS Omega 2021, 6, 33224−33230

(56) Drezner, Y.; Berger, S.; Hefetz, M. A correlation between microstructure, composition and optical transparency of CVD-ZnS. *Mater. Sci. Eng.: B* **2001**, *87*, 59−65.
(57) Pappas, J. M.; Dong, X. Direct 3D Printing of Silica Doped Transparent Magnesium Aluminate Spinel Ceramics. *Materials* **2020**, *13*, 4810.
(58) Morita, K.; Kim, B.-N.; Hiraga, K.; Yoshida, H. Fabrication of transparent $MgAl_2O_4$ spinel polycrystal by spark plasma sintering processing. *Scr. Mater.* **2008**, *58*, 1114−1117.
(59) Furuse, H.; Horiuchi, N.; Kim, B.-N. Transparent non-cubic laser ceramics with fine microstructure. *Sci. Rep.* **2019**, *9*, 10300−10307.
(60) Roy, S.; Lingertat, H.; Brecher, C.; Sarin, V. Optical properties of anisotropic polycrystalline Ce^{3+} activated LSO. *Opt. Mater.* **2013**, *35*, 827−832.
(61) Kim, B.-N.; Hiraga, K.; Morita, K.; Yoshida, H.; Miyazaki, T.; Kagawa, Y. Microstructure and optical properties of transparent alumina. *Acta Mater.* **2009**, *57*, 1319−1326.
(62) Zhang, H.; Yang, J.; Gray, S.; Brown, J. A.; Ketcham, T. D.; Baker, D. E.; Carapella, A.; Davis, R. W.; Arroyo, J. G.; Nolan, D. A. Transparent Er^{3+}-doped Y_2O_3 ceramics with long optical coherence lifetime. *ACS Omega* **2017**, *2*, 3739−3744.
(63) Lempicki, A.; Brecher, C.; Szupryczynski, P.; Lingertat, H.; Nagarkar, V. V.; Tipnis, S. V.; Miller, S. R. A new lutetia-based ceramic scintillator for X-ray imaging. *Nucl. Instrum. Methods Phys. Res., Sect. A* **2002**, *488*, 579−590.
(64) Sabet, H.; Bhandari, H. B.; Kudrolli, H.; Nagarkar, V. V. Fabrication of X-ray/gamma-ray detector by growth of micro-columnar CsI: Tl onto silicon photomultipliers. *Phys. Procedia* **2012**, *37*, 1523−1530.
(65) van Breemen, A. J. J. M.; Simon, M.; Tousignant, O.; Shanmugam, S.; van der Steen, J.-L.; Akkerman, H. B.; Kronemeijer, A.; Ruetten, W.; Raaijmakers, R.; Alving, L.; Jacobs, J.; Malinowski, P. E.; de Roose, F.; Gelinck, G. H. Curved digital X-ray detectors. *npj Flex. Electron.* **2020**, *4*, 22−28.
(66) Zhao, J.; Zhao, L.; Deng, Y.; Xiao, X.; Ni, Z.; Xu, S.; Huang, J. Perovskite-filled membranes for flexible and large-area direct-conversion X-ray detector arrays. *Nat. Photonics* **2020**, *14*, 612−617.

https://doi.org/10.1021/acsomega.1c05962
ACS Omega 2021, 6, 33224−33230